Mission Profile-Based System-Level Reliability Prediction Method for Modular Multilevel Converters

Yi Zhang, *Student Member, IEEE*, Huai Wang, *Senior Member, IEEE*, Zhongxu Wang, *Student Member, IEEE*, Frede Blaabjerg, *Fellow, IEEE*, and Maryam Saeedifard, *Senior Member, IEEE*

***Abstract*—This article proposes a mission profile-based reliability prediction method for modular multilevel converters (MMCs). It includes key modeling steps, such as long-term mission profile, analytical power loss models, system-level and component-level thermal modeling, lifetime modeling, Monte Carlo analysis, and redundancy analysis. Thermal couplings and uneven thermal stresses among submodules are considered. A case study of a 15-kVA downscale MMC has been used to demonstrate the proposed method and validate the theoretical analysis. The outcomes serve as a first step for developing realistic reliability analysis and model-based design methods for full-scale MMCs in practical applications.**

***Index Terms*—Modular multilevel converters (MMCs), power losses, reliability, redundancy, thermal analysis.**

I. INTRODUCTION

MODULAR multilevel converters (MMCs) have distinctive features like modularity, scalability, superior harmonic performance, low switching stresses [1], etc. However, some reliability issues are still challenging its further applications. MMCs are large scale and complex systems. Hundreds or thousands of components, including insulated-gate bipolar transistors (IGBTs) and capacitors, must operate properly. The industry surveys reveal that IGBTs and capacitors contribute to over 50% failures in power electronic systems [2]. Failure of a single critical device might lead to shut down of the whole system and impair its economic revenues. Accordingly, previous studies propose many solutions to improve its reliability, such as redundancies [3], fault-tolerant controls [4], and sizing components with excessive design margins (e.g., components with large safe operating areas, and massive heatsinks, etc.). Nonetheless, the design constraints in cost and efficiency impose significant challenges on excessive utilization of redundancies and design margins. To satisfy the stringent reliability requirements while limiting the cost, the system-level reliability prediction of the MMC is significant in terms of designs and economic analysis.

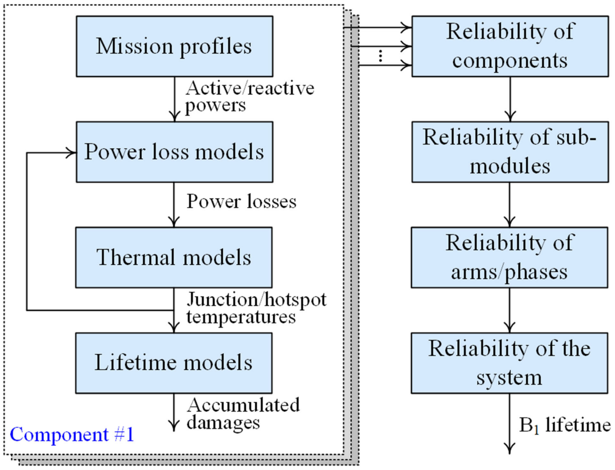

Fig. 1. Reliability evaluation flowchart for hardware wear-out failure probability analysis for the MMC.

Recently, the reliability prediction of MMC has attracted wide attention, such as those presented in [5]–[7]. Many of those reliability predictions rely on constant failure rates of components provided in the Military-Handbook-217F [8]. The constant failure rates describe large-population statistics of random failures, which are limited for MMCs with a small amount of commissioned projects and insufficient long-term usage data. Although the accelerated factors under different conditions have been considered in [7], the failure rate data still do not differentiate technologies and manufacturers. Moreover, wear-out failures are not considered. To design an MMC to fulfill a specific serve lifetime, the failure due to component wear-out should be limited to an acceptable level. From this perspective, the constant-failure-rate methods still have gaps in designing an MMC to achieve a specific reliability target with compromised design margins and costs. Additionally, physics-of-failure methods have been presented to consider the component-level reliability of MMCs in [9] and [10]. However, considering the numerous components, submodules (SMs), and complicated redundancies, it is still challenging to apply the same method to do the system-level reliability of the MMC.

As shown in Fig. 1, the system-level reliability prediction of the MMC involves reviewing from components, SMs to the entire system. The power loss models and thermal models are

---

Manuscript received August 5, 2019; revised October 29, 2019; accepted November 27, 2019. Date of publication December 3, 2019; date of current version March 13, 2020. This work was supported by the Innovation Fund Denmark through the Advanced Power Electronic Technology and Tools project. Recommended for publication by Associate Editor M. Nawaz. *(Corresponding author: Yi Zhang.)*

Y. Zhang, H. Wang, Z. Wang, and F. Blaabjerg are with the Department of Energy Technology, Aalborg University, 9100 Aalborg, Denmark (e-mail: yiz@et.aau.dk; hwa@et.aau.dk; zho@et.aau.dk; fbl@et.aau.dk).

M. Saeedifard is with the School of Electrical and Computer Engineering, Georgia Institute of Technology, Atlanta, GA 30332 USA (e-mail: maryam@ece.gatech.edu).

Color versions of one or more of the figures in this article are available online at http://ieeexplore.ieee.org.

Digital Object Identifier 10.1109/TPEL.2019.2957826

prerequisites in the process and meanwhile associated with many challenges.

First, from the perspective of system-level reliability analysis, power loss evaluation requires computational efficiency, involving all critical components, and utilization of system-level specifications only. The power losses of the MMC have been discussed by numerical simulations [11], which have the advantage of considering sophisticated control strategies. However, different cases rely on the modification of simulation parameters. When comparing reliable performance of different design schemes, simulation-based methods are challenging to quickly and automatically scan many parameters. Alternatively, analytical power losses models [12]–[14] outperform in the aspect of computational efficiency and easy parameter-changing. The aforementioned analytical methods mostly focus on the power semiconductor devices. Capacitors, inductors and bleeding resistors (in parallel with the capacitors), which contribute to non-negligible power losses and system-level degradation, have been rarely considered. Notably, the available information for reliability evaluation is limited in the initial design stage, which requires the power loss models with only system-level specifications (e.g., grid voltages, active and reactive powers, etc.).

Second, thermal models are essential to evaluate the reliability of the MMC. As one of the critical components, the thermal behaviors of IGBT modules have been reported in [9], [15]–[18]. The typically used thermal models are one-dimensional (1-D) RC lumped networks, which are normally provided by the manufacturer in the datasheet [19]. However, thermal cross coupling (TCC) effects occur when multiple chips/devices exist within the same package, and even if different modules are mounted on the same assembly. The 1-D thermal model fails to consider the TCC effects and might result in underestimated thermal stresses. Apart from IGBT modules, capacitors are usually regarded as the bottleneck of power electronics in terms of reliability [20], [21], but their thermal behaviors in the MMC are rarely discussed. In addition to the abovementioned thermal behaviors of devices, system-level thermal behaviors of the MMC have not received much attention. This process involves the impact of cooling systems and many SMs with different local ambient temperatures as well as the TCC effects among them. Thus, a comprehensive system-level thermal model is necessary to take all the abovementioned effects into account.

Some studies have investigated the system-level reliability of other types of converters, such as a dc–dc converter [21] and a PV microinverter [22]. Shen *et al.* [22] considered all TCC effects based on the converter level, but the all devices are assumed to be exposed to the same environmental stresses. The assumption may be reasonable in certain types of systems. However, the complexity level and the overall size of MMC are far beyond those converters have been studied. The assumption of homogeneous local environmental stresses for all the devices is questionable. Moreover, the redundancies of the MMC are also out of the scope of previous studies. Therefore, these limitations highlight the importance of system-level reliability investigation of the MMC.

This article proposes a mission profile-based system-level reliability prediction method for MMCs. The novel aspects of the proposed method are as follows.

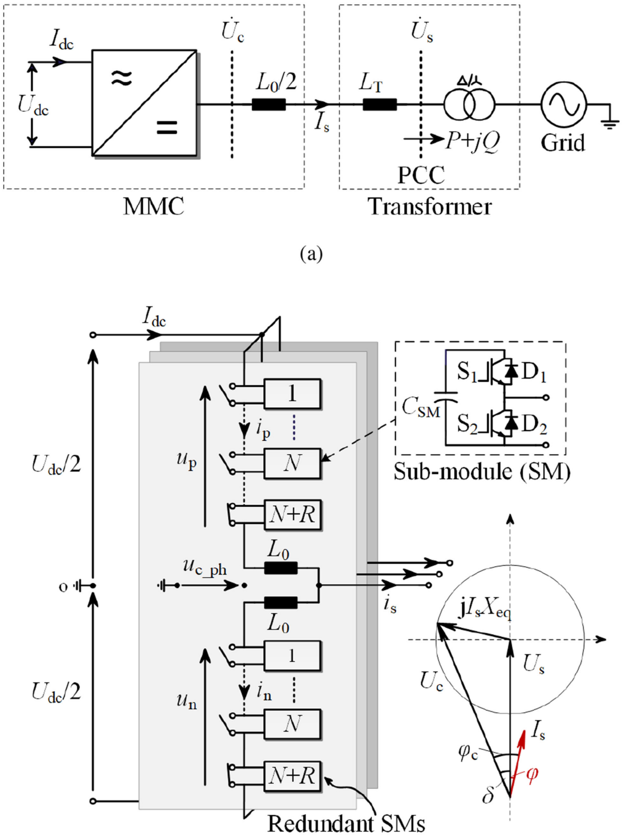

(a)

(b)

Fig. 2. Circuit structure of an MMC. (a) Diagram of the MMC interfaced to the grid. (b) Circuit configuration and the operational vectors.

1) Establish a system-level power loss analytical model covering all critical components in the MMC, which considers the impacts of various parameters and mission profiles.
2) Establish a systematic thermal model for the entire MMC, considering TCC effects and uneven thermal stresses from components to the system.
3) Assess the system-level reliability of the MMC by considering different stresses in various SMs and redundancies. Potential limitations applying the proposed methods to a full-scale MMC are also clarified.

The outcomes serve as a first step for developing realistic reliability analysis and model-based design methods for full-scale MMCs in practical applications.

II. CONFIGURATION OF THE MMC SYSTEM AND A DOWN-SCALE PROTOTYPE

A. System Description

A schematic of a three-phase MMC interfaced to an ac system is shown in Fig. 2, where L_0 is the arm inductor and L_T is the leakage inductance of the transformer. Notably, the leakage inductance is typically around 0.14 p.u. [23]. The exclusion of this portion of reactive power consumption might result in underestimated device stresses. Thereby, the equivalent phase inductance L_{eq} is $L_{eq} = L_T + L_0/2$. In the interior of the MMC, each phase is comprised of two arms, where each arm consists of N identical normal SMs, R redundant SMs and an arm inductor. Each SM is a half-bridge circuit with two IGBTs (denoted as S_1 and S_2) and two diodes (D_1 and D_2).

As shown in Fig. 2, the grid voltage and the line-to-line voltage at the converter terminal are expressed as

$$\dot{U}_{\mathrm{s}} = \hat{U}_{\mathrm{s}}\angle 0^\circ, \quad \dot{U}_{\mathrm{c}} = \hat{U}_{\mathrm{c}}\angle\delta \tag{1}$$

where $\hat{U}_{\mathrm{s}}$ and $\hat{U}_{\mathrm{c}}$ are the amplitudes of the grid voltage at the point of common coupling (PCC) and the converter ac voltage, respectively, and δ is the angle between them.

The relationship between the converter root mean square (rms) ac voltage U_{c} and the phase voltage amplitude $\hat{U}_{\mathrm{c\_ph}}$ is expressed as

$$U_{\mathrm{c}} = \frac{\sqrt{3}}{\sqrt{2}}\hat{U}_{\mathrm{c\_ph}} = \frac{\sqrt{3}}{2\sqrt{2}} m U_{\mathrm{dc}} \tag{2}$$

where m is the modulation index ($m = 2\hat{U}_{\mathrm{c\_ph}}/U_{\mathrm{dc}}$).

Based on [24], the active/reactive power at the PCC is

$$\begin{cases} P = \frac{U_{\mathrm{s}} U_{\mathrm{c}} \sin\delta}{X_{\mathrm{eq}}} \\ Q = \frac{U_{\mathrm{s}}(U_{\mathrm{c}}\cos\delta - U_{\mathrm{s}})}{X_{\mathrm{eq}}} \end{cases} \tag{3}$$

where X_{eq} is the impedance of the phase inductance L_{eq}.

Solving (2) and (3), the angle δ and the modulation index m are derived as

$$\delta = \arctan\left(\frac{P X_{\mathrm{eq}}}{U_{\mathrm{s}}^2 + Q X_{\mathrm{eq}}}\right) \tag{4}$$

$$m = \frac{2\sqrt{2}\left(Q X_{\mathrm{eq}} + U_{\mathrm{s}}^2\right)}{\sqrt{3} U_{\mathrm{dc}} U_{\mathrm{s}} \cos\delta}. \tag{5}$$

The angle δ and the modulation index m mainly depend on the P/Q set points. It indicates that both the two parameters are not changed freely when the MMC is connected to the grid.

Therefore, the phase voltage at the converter terminal and the ac current are expressed according to Fig. 2, which are

$$u_{\mathrm{c\_ph}}(t) = m\frac{U_{\mathrm{dc}}}{2}\sin(\omega t) \tag{6}$$

$$i_{\mathrm{s}}(t) = \sqrt{2} I_{\mathrm{s}} \sin(\omega t - \varphi_{\mathrm{c}}) \tag{7}$$

where φ_{c} is the phase angle given by the converter ac voltage, which has $\varphi_{\mathrm{c}} = \delta + \varphi$, and φ is the phase angle between the grid voltage U_{s} and I_{s} at the PCC, revealing the power factor.

In the steady state, the arm currents mainly consist of a sinusoidal component and a dc bias, which are expressed as

$$\begin{cases} i_{\mathrm{p}}(t) = \frac{\hat{I}_{\mathrm{s}}}{2}\left[k + \sin(\omega t - \varphi_{\mathrm{c}})\right] \\ i_{\mathrm{n}}(t) = \frac{\hat{I}_{\mathrm{s}}}{2}\left[k - \sin(\omega t - \varphi_{\mathrm{c}})\right] \end{cases} \tag{8}$$

where k is the current ratio ($k = \frac{I_{\mathrm{dc}}}{3} \big/ \frac{\hat{I}_{\mathrm{s}}}{2} = \frac{1}{2} m \cos\varphi_{\mathrm{c}}$).

According to Kirchhoff's voltage law and (6), the upper and lower arm voltages are given by

$$\begin{cases} u_{\mathrm{p}} = \frac{U_{\mathrm{dc}}}{2} - u_{\mathrm{c\_ph}} = \frac{1}{2}\left[1 - m\sin(\omega t)\right] U_{\mathrm{dc}} \\ u_{\mathrm{n}} = \frac{U_{\mathrm{dc}}}{2} + u_{\mathrm{c\_ph}} = \frac{1}{2}\left[1 + m\sin(\omega t)\right] U_{\mathrm{dc}}. \end{cases} \tag{9}$$

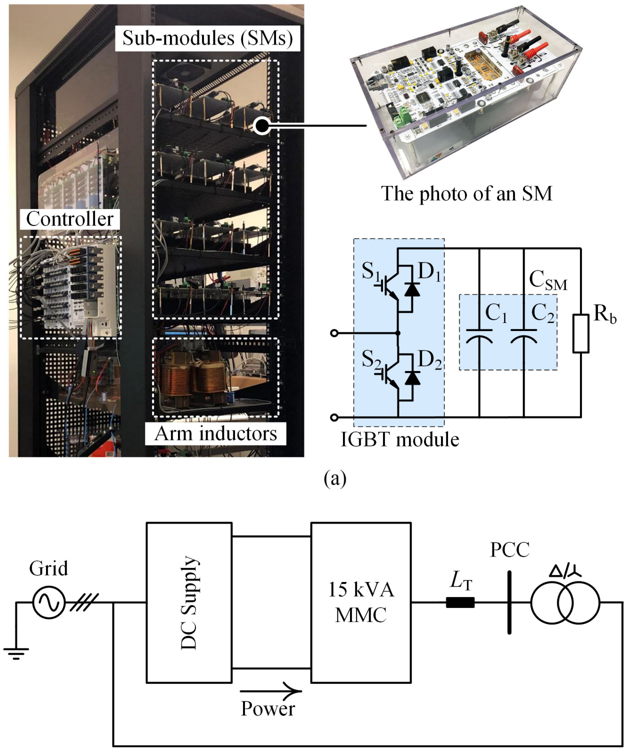

(a)

(b)

Fig. 3. 15-kVA down-scale MMC prototype. (a) Photo of the platform along with the SM circuit. (b) Circuit configuration of the setup.

According to [25], the insertion probability of the upper and lower arms are denoted by N_{p} and N_{n}, that is

$$\begin{cases} N_{\mathrm{p}} = \frac{1}{2}\left[1 - m\sin(\omega t)\right] \\ N_{\mathrm{n}} = \frac{1}{2}\left[1 + m\sin(\omega t)\right]. \end{cases} \tag{10}$$

So far, all the variables inside the MMC (e.g., modulation index, arm voltages/currents) have established the analytical relationships according to the P/Q set points of the PCC.

B. Description of the Down-Scale MMC Prototype

In this work, a 15 kVA down-scale MMC prototype has been built for experimental verification, as shown in Fig. 3. There are 18 normal and six redundant SMs in total. In each SM, the capacitor bank is comprised of two capacitors connected in parallel. The detailed specifications are listed in Table I. In particular, although the MMC-based HVdc systems commonly employ high-power film capacitors and air-core inductors, the down-scale prototype utilizes the commercial Aluminum electrolytic capacitors (Al-Caps) and iron-core inductors due to the volume and power density limitations. It is worth noticing that the Al-Caps and iron-core inductors also offer advantages for medium-power MMC applications [26]. Moreover, a comparison of different component sizes is also discussed in Section VI.

As shown in Fig. 4, the P/Q capability circle shows that selected operational P/Q ranges are located within limits. In

TABLE I
SPECIFICATIONS AND PARAMETERS OF A DOWN-SCALE MMC PROTOTYPE

Parameters and symbols	Values and units
Nominal apparent power S_N	15 kVA
Nominal active power P_N	13.5 kW
DC bus voltage U_{dc}	900 V
Switching frequency f_{sw}	1.5 kHz
Leakage reactance of the transformer L_T	4 mH (0.12 p.u.)
Arm reactance L_0	4 mH (0.12 p.u.)
SM capacitance $C_{SM} = C_1 + C_2$	400 V/820 μF ×2
Grid line voltage at PCC U_s	380 V
Number of normal SMs per arm N	3
Number of redundant SMs per arm R	1
Bleeding resistor of each SM R_b	12 kΩ
IGBT module	1.2 kV/50 A (F4-50R12KS4)

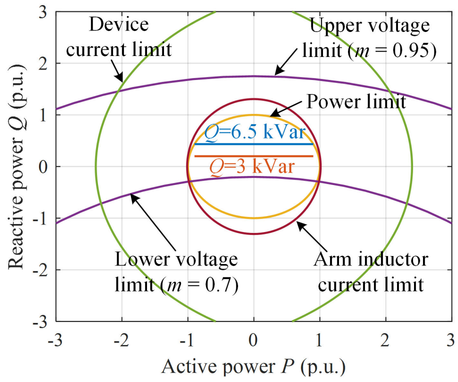

Fig. 4. P/Q capability graph of the down-scale MMC in Fig. 3.

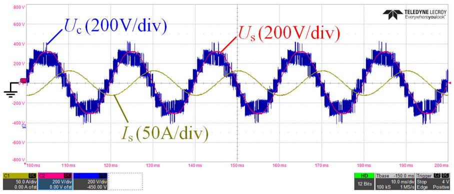

Fig. 5. Steady-state MMC waveforms when $P = 13.5$ kW and $Q = 6.5$ kVar (U_s: the grid voltage, U_c: the converter ac voltage, and I_s: the current).

addition, the steady-state waveforms in Fig. 5 verify proper operation of the converter under nominal conditions ($P = 13.5$ kW and $Q = 6.5$ kVar).

III. CLASSIFICATION OF THE POWER LOSSES OF THE CRITICAL COMPONENTS

In the initial design of an MMC, the power losses of many component candidates need to be evaluated quickly. This section provides analytical power loss models for the critical components (i.e., IGBTs, capacitors, inductors, and bleeding resistors). The analytical models utilize only grid-level information (e.g., grid voltages, P/Q set points at PCC, etc.), which is usually accessible in the initial design stage. Moreover, the selected components are measured to reveal the uneven parameters in practice, which will be taken into account by subsequent reliability evaluation. Finally, the theoretical power loss formulas and experimental results are also compared.

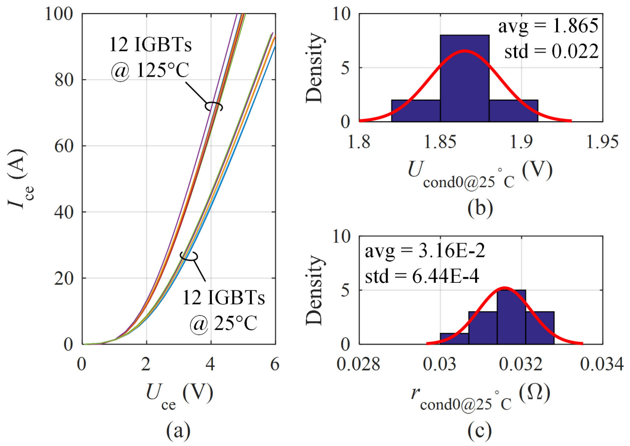

Fig. 6. Measured conduction losses of 12 IGBT modules. (a) Output characteristic of the IGBT. (b) Obtained $U_{cond0@25^\circ C}$ and its distributions. (c) Obtained $r_{cond0@25^\circ C}$ and its distributions.

TABLE II
MEASURED POWER LOSS COEFFICIENTS FOR THE SELECTED IGBT MODULES
(AVG: AVERAGE VALUES, STD: STANDARD DEVIATIONS)

		IGBT		Diode	
		AVG	STD	AVG	STD
$U_{cond0@T_{ref}}$	[V]	1.87	2.2E-2	1.31	2.5E-2
$r_{cond0@T_{ref}}$	[Ω]	3.16E-2	6.4E-4	1.46E-2	5.2E-4
K_{T1}	[V/°C]	2.70E-3	1.7E-4	-3.3E-3	4.2E-4
K_{T2}	[Ω/°C]	9.73E-5	1.1E-5	1.82E-5	2.9E-6
K_i	[1]	1.30	2.2E-2	3.32E-1	5.5E-3
K_u	[1]	1.33	2.2E-2	1.72	2.9E-2
K_{sw}	[1/°C]	2.76E-3	4.6E-5	1.84E-2	3.1E-4

*for IGBT, $E_{swref} = 0.72$ mJ, $I_{ref} = 20$ A, $U_{ccref} = 300$ V;
*for Diode, $E_{swref} = 0.26$ mJ, $I_{ref} = 20$ A, $U_{ccref} = 300$ V.

A. *Power Losses of the IGBT Modules*

In the down-scale prototype, a 1200 V/50 A IGBT module is used, where the composition of power losses are conduction and switching losses. According to [27], the conduction losses of the IGBT/diode are calculated by

$$\begin{aligned} P_{cond} = & \left|I_{avg}\right| \left[U_{cond0@T_{ref}} + K_{T1}\left(T_j - T_{ref}\right)\right] \\ & + I_{rms}^2 \left[r_{cond0@T_{ref}} + K_{T2}\left(T_j - T_{ref}\right)\right] \end{aligned} \tag{11}$$

with $U_{cond0@T_{ref}}$, $r_{cond0@T_{ref}}$, K_{T1} and K_{T2} being the coefficients obtained experimentally, as shown in Fig. 6 and Table II. The reference temperature is $T_{ref} = 25\,^\circ$C and T_j is the junction temperature. In addition, I_{avg} and I_{rms} are the average and the rms currents flowing through the devices. The switching energy dissipations $E_{sw} = E_{on} + E_{off}$ for the IGBT, and the reverse recovery energy per pulse $E_{sw} = E_{rec}$ for the freewheeling diode for the current I are given by

$$E_{sw} = E_{swref}\left(\frac{I}{I_{ref}}\right)^{K_i}\left(\frac{U_{SM}}{U_{ccref}}\right)^{K_u}\left[1 + K_{sw}\left(T_j - T_{ref}\right)\right] \tag{12}$$

with I_{ref}, U_{ccref}, and E_{swref} being the nominal test conditions. K_i, K_u, and K_{sw} are the coefficients obtained from the measurements, as shown in Fig. 7 and Table II. U_{SM} is the SM capacitor voltage.

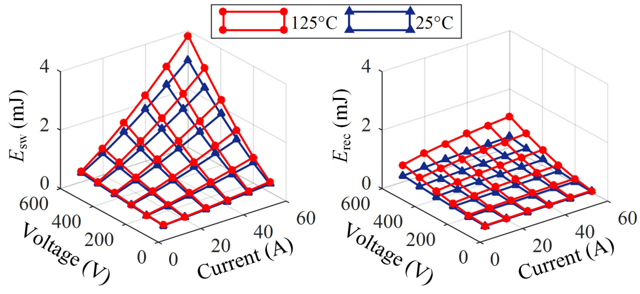

(a) (b)

Fig. 7. Measured switching energy dissipations in the IGBT modules. (a) IGBTs. (b) Diodes.

Subsequently, the average switching losses are

$$P_{\text{sw\_S/D}} = \frac{1}{T}\sum_{t_0}^{t_0+T} E_{\text{sw}}\left(i_{\text{CE/f}}\right) \tag{13}$$

where $P_{\text{sw\_S/D}}$ and $i_{\text{CE/f}}$ are the average switching losses and the instantaneous device currents for IGBTs or diodes, respectively.

Based on (11), the key task to calculate the power losses of the IGBT module is to find the instantaneous, the average and the rms currents of the power device. Solving (8), the zero crossing points of the arm current are at

$$\begin{cases} \omega t_1 = -\alpha + \varphi_{\text{c}} \\ \omega t_2 = \pi + \alpha + \varphi_{\text{c}} \end{cases} \text{ where } \alpha = \arcsin(k) \tag{14}$$

when the arm current is positive (i.e., $\omega t_1 \leq \omega t < \omega t_2$), it flows through the devices D_1 and S_2. On the contrary, the arm current passes through the devices S_1 and D_2 when it is negative. The instantaneous, the average and the rms currents of the device S_1 are calculated as

$$i_{\text{CE\_S1}} = \begin{cases} 0, & 2\pi + \omega t_1 \leqslant \omega t < \omega t_2 \\ N_{\text{p}} i_{\text{p}}, & \omega t_2 \leqslant \omega t < 2\pi + \omega t_1 \end{cases} \tag{15}$$

$$I_{\text{S1\_avg}} = \frac{1}{2\pi}\int_{\omega t_2}^{2\pi+\omega t_1} N_{\text{p}} i_{\text{p}} d\omega t = \frac{\hat{I}_{\text{s}}}{4\pi}\left(k^2 - 1\right)\cos\alpha \tag{16}$$

$$I_{\text{S1\_rms}}^2 = \frac{\hat{I}_{\text{s}}^2}{16\pi}\left[\left(\frac{1}{2} - k^2\right)(\pi - 2\alpha) - \frac{k}{3}\cos(3\alpha)\right]. \tag{17}$$

The device currents of S_2, D_1, and D_2 are obtained similarly as listed in Table III. Substituting the device currents into (11) and (13), the average power losses of the power devices are obtained.

Based on the established models, the power losses under various P/Q set points are shown in Fig. 8. When $P > 0$ (inverter mode), the dc-bias current flows through the devices S_2 and D_1, which leads to higher power losses. On the contrary, devices D_2 and S_1 dominate the power losses when $P < 0$ (rectifier mode). Moreover, when the reactive power is reduced from 6.5 to 3 kVar, the power losses of the all power devices are alleviated correspondingly.

TABLE III
AVERAGE AND RMS CURRENTS OF THE POWER DEVICES IN AN SM OF THE MMC

	Average current (A)
S_1	$\frac{\hat{I}_{\text{s}}}{4\pi}\left(k^2 - 1\right)\cos\alpha$
D_1	$\frac{\hat{I}_{\text{s}}}{4\pi}\left(1 - k^2\right)\cos\alpha$
S_2	$\frac{\hat{I}_{\text{s}}}{4\pi}\left[(\pi + 2\alpha)k + \left(1 + k^2\right)\cos\alpha\right]$
D_2	$\frac{\hat{I}_{\text{s}}}{4\pi}\left[(\pi - 2\alpha)k - \left(1 + k^2\right)\cos\alpha\right]$
	The power of RMS current (A^2)
S_1	$\frac{\hat{I}_{\text{s}}^2}{16\pi}\left[\left(\frac{1}{2} - k^2\right)(\pi - 2\alpha) - \frac{k}{3}\cos(3\alpha)\right]$
D_1	$\frac{\hat{I}_{\text{s}}^2}{16\pi}\left[\left(\frac{1}{2} - k^2\right)(\pi + 2\alpha) + \frac{k}{3}\cos(3\alpha)\right]$
S_2	$\frac{\hat{I}_{\text{s}}^2}{16\pi}\left[\left(\frac{1}{2} + 3k^2\right)(\pi + 2\alpha) + 6k\cos\alpha - \frac{k}{3}\cos(3\alpha)\right]$
D_2	$\frac{\hat{I}_{\text{s}}^2}{16\pi}\left[\left(\frac{1}{2} + 3k^2\right)(\pi - 2\alpha) - 6k\cos\alpha + \frac{k}{3}\cos(3\alpha)\right]$

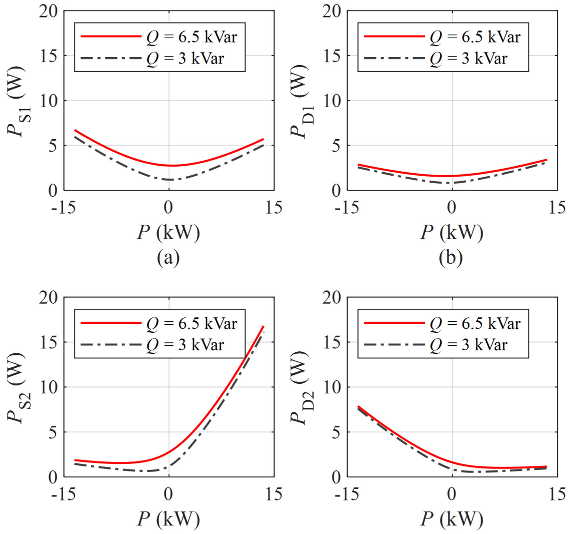

(a) (b)

(c) (d)

Fig. 8. Power losses of the semiconductor devices in an SM ($P > 0$ inverter mode, $P < 0$ rectifier mode): (a) S_1, (b) D_1, (c) S_2, and (d) D_2.

B. Power Losses of Capacitors

According to [20], the power losses of a capacitor are expressed by the rms capacitor current $I_{\text{cap\_rms}}$ and capacitor series resistance ESR_{cap}, which are expressed by

$$P_{\text{cap}} = \sum_{\omega=0}^{\infty} I_{\text{cap\_rms}}^2(\omega) \cdot \text{ESR}_{\text{cap}}(\omega). \tag{18}$$

The capacitor current of the MMC mainly consists of the first- and the second-order components [25], whose amplitudes are

$$\hat{I}_{\text{cap}}(\omega) = \frac{\hat{I}_{\text{s}}}{4}\sqrt{m^2k^2 - 2m\cos\varphi_{\text{c}} + 1} \tag{19}$$

$$\hat{I}_{\text{cap}}(2\omega) = \frac{m\hat{I}_{\text{s}}}{8}. \tag{20}$$

The measured capacitor series resistance versus frequency is shown in Fig. 9, which decreases progressively with the frequency with sensible differences for those 80 capacitors. The measured ESR_{cap} is 115 mΩ (50 Hz) and 89.6 mΩ (100 Hz) on the average, respectively

Substituting (19), (20), and the ESR_{cap} into (18), the corresponding capacitor losses are obtained, as shown in Fig. 10. The first- and second-order capacitor currents are symmetrical

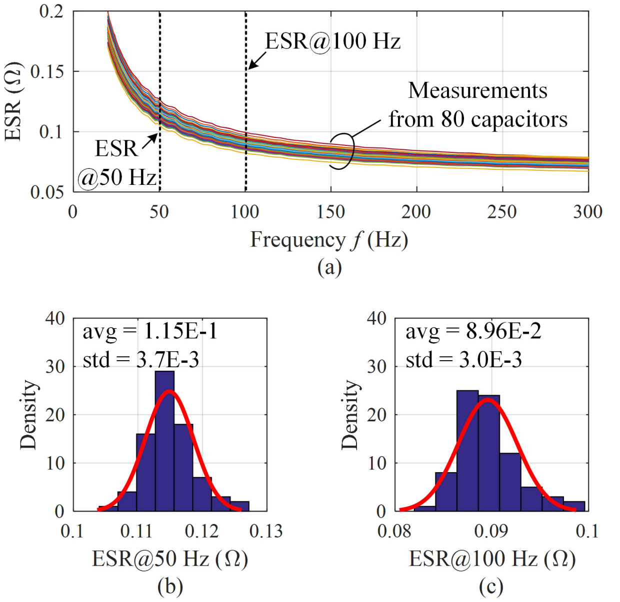

(a)

(b) (c)

Fig. 9. Measurements of 80 capacitor series resistances under different frequencies. (a) Capacitor series resistance and (b) the distribution of $\mathrm{ESR_{cap}}$ at 50 Hz. (c) $\mathrm{ESR_{cap}}$ at 100 Hz.

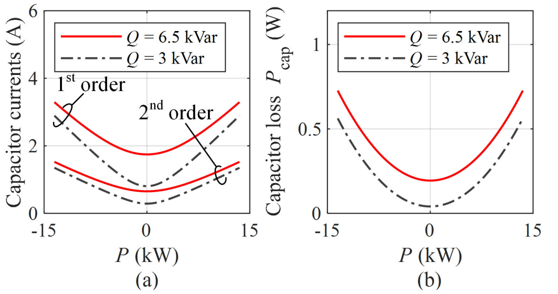

(a) (b)

Fig. 10. Capacitor currents and power losses. (a) First- and second-order capacitor currents. (2) Capacitor power losses.

with respect to $P = 0$-axis. However, the first-order capacitor current is approximately four times the second order, indicating that the capacitor power losses are mainly produced by the first-order component. Moreover, both the capacitor currents and the power losses decrease as the reactive power demand decreases.

C. Power Losses of the Arm Inductors

The down-scale prototype uses iron-core arm inductors. The inductor power losses P_{armL} consist of winding losses P_{w} and core losses P_{core}. The winding losses depend on the resistance of each conducting element and the rms current that flows through it, which are

$$P_{\mathrm{w}} = \sum_{\omega=0}^{\infty} i^2_{\mathrm{p/n\_rms}}(\omega)\, R_{\mathrm{sL}}(\omega) = \frac{\hat{I}_s^2 k^2}{4} R_{\mathrm{sL\_dc}} + \frac{\hat{I}_s^2}{8} R_{\mathrm{sL\_ac}} \quad (21)$$

where $i_{\mathrm{p/n\_rms}}$ is the rms value of the upper/lower arm current, and R_{sL} is the equivalent series resistance of the arm inductor. In the six arm inductors, the measured R_{sL} increases against the frequency as shown in Fig. 11, where the resistances are 64.4 mΩ (0 Hz) and 66.9 mΩ (50 Hz) on average, respectively.

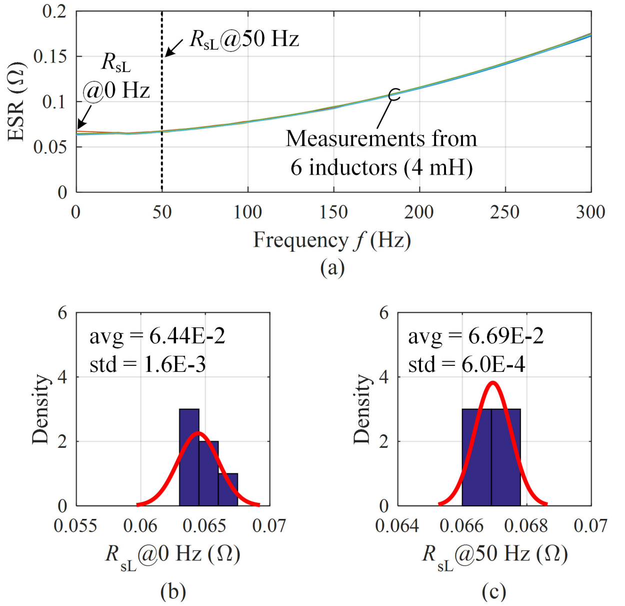

(a)

(b) (c)

Fig. 11. Measured equivalent series resistance of six arm inductors. (a) Inductor series resistances and (b) the parameter distribution at 0 Hz. (c) The distribution at 50 Hz.

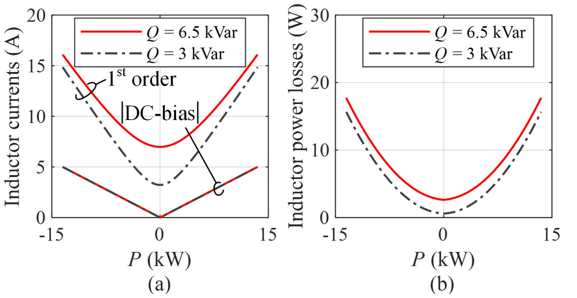

(a) (b)

Fig. 12. Arm inductor currents and power losses: (a) dc and 50-Hz components of the arm current, (b) power losses of an arm inductor.

According to [28], the core losses of the arm inductors are excited by the sinusoidal current with a dc-bias, which are

$$P_{\mathrm{core}} = \left(C_{\mathrm{dc}} K_{\mathrm{h}} f \hat{B}^2 + K_{\mathrm{c}} f^2 \hat{B}^2 + K_{\mathrm{e}} f^{1.5} \hat{B}^{1.5}\right) \cdot V_{\mathrm{c}} \quad (22)$$

where $\hat{B}$ is the amplitude of the ac flux, K_{h}, K_{c}, and K_{e} are the hysteresis, the eddy current and the excess core loss coefficients, respectively. V_{c} is the core volume, and C_{dc} considers the impact of the dc-bias current.

The arm current and power losses are shown in Fig. 12. The arm current is dominated by the first-order component, as shown in Fig. 12(a). Meanwhile, the dc component of the arm current is independent of reactive power. Finally, the power losses of the arm inductor are correspondingly shown in Fig. 12(b).

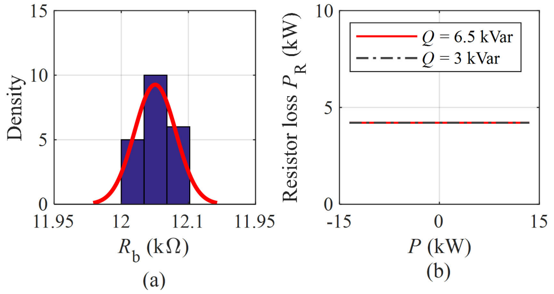

Fig. 13. Parameter distribution and the power losses of the bleeding resistors. (a) Measured resistance distribution. (b) Power losses of the bleeding resistor under different P/Q set points.

D. Power Losses of the Bleeding Resistors

The bleeding resistors are connected in parallel with the SM capacitors. The power losses of a bleeding resistor are voltage dependent as

$$P_{\mathrm{R}} = \frac{U_{\mathrm{SM}}^2}{R_{\mathrm{b}}}. \tag{23}$$

According to the measured parameter distribution of the selected bleeding resistors shown in Fig. 13(a), the average resistance is 12.03 kΩ. Due to the mean value of the capacitor voltage, which is independent of the active/reactive powers, the corresponding power losses are almost constant under different P/Q values, which are shown in Fig. 13(b).

E. Experimental Verifications

The power losses of the aforementioned components are measured by the Newtons power analyzer PPA5500, and the measured results are compared to the theoretical values, as shown in Fig. 14. Since it is difficult to measure the power losses of a single power semiconductor chip, the entire IGBT module is measured. The total power losses of the four power devices (i.e., S_1, S_2, D_1, and D_2) are shown in Fig. 14(a). The measurements coincide with the theoretical values with a maximum error of 5.4%. Next, a comparison of the measured capacitor power losses and the theoretical values are shown in Fig. 14(b). The capacitor power losses are relatively small, where the maximum value is roughly 0.8 W. Furthermore, the power losses of the arm inductor are shown in Fig. 14(c). The maximum error is up to 50.1% when $P = 0$ kW. The differences are probably from the core loss model without considering the harmonics. When $P = 0$ kW, the inductor current is minimal. The error of core losses due to harmonics accounts for a large part, which leads to a large error. However, the difference of around 3 W under the condition is still acceptable. Moreover, MMC applications usually utilize air-core inductors. The error from core losses contributes to a minor effect in real applications.

So far, the system-level power loss model has been established for the MMC. Both the device parameters and mission profiles (i.e., P/Q set points at PCC) are considered. The corresponding outcomes provide the basis for the next thermal analysis and lifetime prediction.

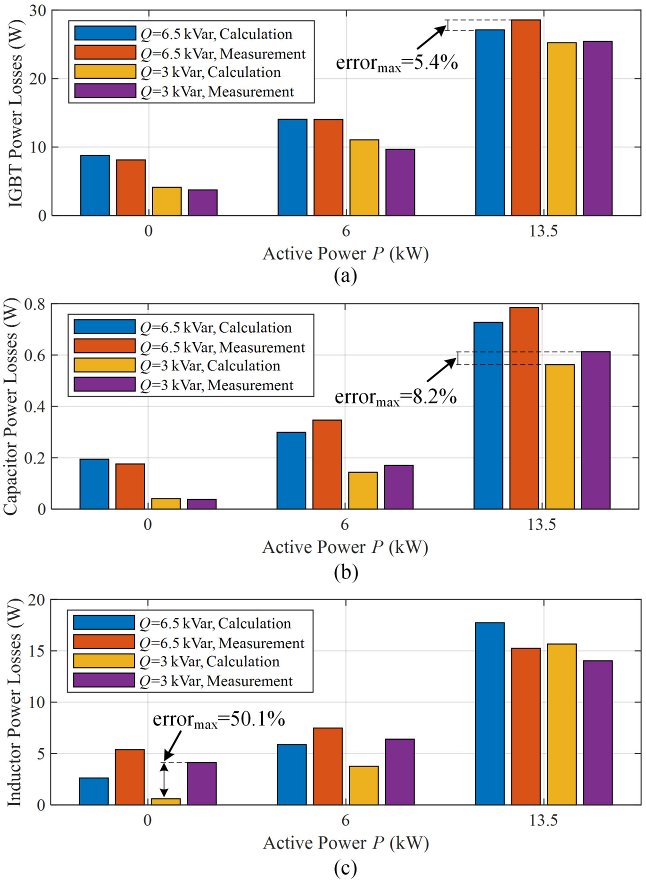

Fig. 14. Comparison of the theoretical power losses and the measurements: (a) IGBT module, (b) capacitor and (c) arm inductor. (measurements are carried under the ambient temperature of 28 °C and operated after one hour.)

IV. SYSTEM-LEVEL THERMAL MODELING

A typical MMC system usually consists of thousands of components and SMs, which is challenging to establish a system-level thermal modeling. As shown in Fig. 15, the layout of the down-scale MMC prototype is composed of 24 SMs and six arm inductors. From the bottom to the top, each SM is given a unique label as $\{\mathrm{SM1}, \mathrm{SM2}, \ldots, \mathrm{SM24}\}$. The environmental cooling air is imported from the bottom and backside grilles. Then, the hot air exhausts via fans on the top of the cabinet. In this section, a system-level thermal model is proposed based on the prototype via two aspects, as shown in Fig. 16. First, the junction/hotspot-to-local ambient thermal models of each device are established. The TCC effects consider the mutual influences among different semiconductor chips, capacitors, etc. In addition, the previous studies usually assume that the local ambient temperatures of all SMs are identical to the environmental global ambient temperature [9], [29], or all the devices are exposed to a homogeneous local ambient temperature. However, for the MMC with many SMs, although the power losses of SMs are evenly distributed, the inner temperature of the cabinet is not homogeneous in practice. This means that the SMs might bear different local environmental stresses. From this point, the second part of the thermal model depicts the relationship between the local ambient temperature of each SM and the global

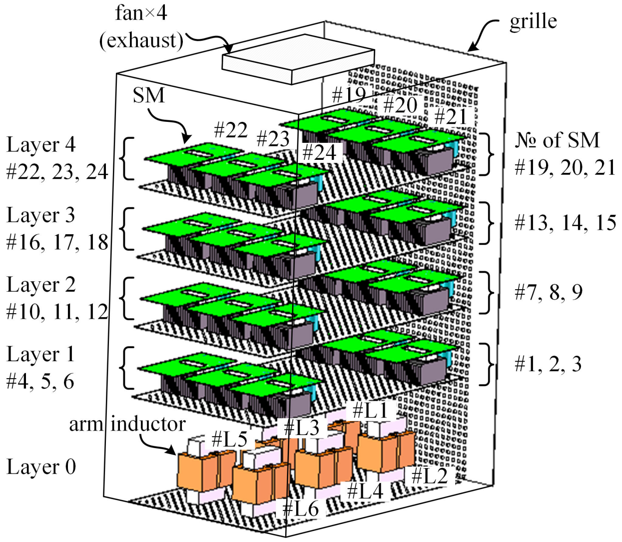

Fig. 15. Three-dimensional layout of the down-scale MMC, where cooling air is imported from the bottom and backside grilles then exhausting via the top fans.

ambient temperature. The TCC effects of neighboring SMs and arm inductors are included in the process.

A. Junction/Hotspot-to-Local Ambient Thermal Modeling

As shown in Fig. 17, each SM is comprised of an IGBT module, two capacitors, and a bleeding resistor mainly. In the conventional thermal models (e.g., the datasheet provided thermal model [19]), junction/hotspot temperatures of devices only consider the self-heating effect. However, any device dissipating power produces a temperature rise not only for itself but also all other neighboring devices. The TCC effect from other devices depends on the distance of heat sources and the magnitude of the power generated at heat sources. Thus, the junction/hotspot-to-local ambient thermal model of SM1 is shown in Fig. 16, where the TCC effects among the devices are considered; thus, the thermal model is expressed as

$$\begin{bmatrix} T_{\mathrm{j1}} \\ \vdots \\ T_{\mathrm{j6}} \end{bmatrix} = \begin{bmatrix} Z_{\mathrm{ja1,1}} & \cdots & Z_{\mathrm{ja1,6}} & Z_{\mathrm{ja1,R}} \\ \vdots & \ddots & \vdots & \vdots \\ Z_{\mathrm{ja6,1}} & \cdots & Z_{\mathrm{ja6,6}} & Z_{\mathrm{ja6,R}} \end{bmatrix} \begin{bmatrix} P_1 \\ \vdots \\ P_6 \\ P_{\mathrm{R}} \end{bmatrix} + T_{\mathrm{la1}} \qquad (24)$$

where the subscripts $\{1, 2, \ldots, 6, \mathrm{R}\}$ denote the devices $\{\mathrm{S}_1, \mathrm{S}_2, \mathrm{D}_1, \mathrm{D}_2, \mathrm{C}_1, \mathrm{C}_2, \mathrm{R}_\mathrm{b}\}$, $T_{\mathrm{j1}}, T_{\mathrm{j2}}, \ldots, T_{\mathrm{j6}}$ are the junction or hotspot temperatures, $Z_{\mathrm{ja}i,j}$ are the junction/hotspot-to-local ambient thermal impedances, $P_1, \ldots, P_6, P_{\mathrm{R}}$ are the corresponding power losses, and T_{la1} is the local ambient temperature of SM1. The local ambient temperature is defined as the environmental temperature around the SM.

Both the geometrical structure and the heat transfer (including conduction, convection, and radiation) of the SM are complicated. It is not trivial to analytically obtain the junction/hotspot-to-local ambient thermal impedances. Therefore, finite element method (FEM) simulations with ANSYS/Icepak are conducted based on real dimensions and material properties as shown in Fig. 17(a). The obtained thermal impedances are depicted in Fig. 18. The self-thermal impedance of S_1 (denotes $Z_{\mathrm{ja1,1}}$) peaks at around 1.7 °C/W. Simultaneously, the TCC effect contributes to thermal impedances of 1.2 °C/W for D_1 and D_2, and 1 °C/W for S_2. It reveals that the power losses of the device S_1 also heat the rest of power semiconductor devices. By contrast, the mutual thermal impedances of both capacitors (C_1 and C_2) are almost zero, which means that the temperature variations in the IGBT module do not affect the capacitors. In addition, the self and mutual thermal impedances of the passive component C_2 are shown in Fig. 18(b). The self-thermal impedance of C_2 (i.e., $Z_{\mathrm{ja6,6}}$) has a larger amplitude (5.5 °C/W) than the active devices. The capacitor C_2 also has a significant TCC effect on the parallel-connected capacitor C_1, but is independent of the IGBT module in the SM.

As shown in Fig. 19, the junction and hotspot temperatures of an SM are measured under the local ambient temperature $T_{\mathrm{lamb}} = 28\,^\circ\mathrm{C}$. The device S_2 has the maximum power losses of 16.8 W and corresponding junction temperature is 67 °C. Meanwhile, the power losses of device D_2 are only around 1 W while its junction temperature still has 51 °C. Most of the temperature rise of D_2 comes from the TCC effect of neighboring heat sources. Based on the aforementioned thermal model considering TCC effects, the estimated thermal behaviors closely agree with the measurements. However, the estimated thermal results are largely underestimated by the conventional thermal model without considering the TCC effects. Especially for the devices D_2, C_1, and C_2 with relatively minor power losses, the estimated error is up to 45% based on the conventional thermal model. The comparison verifies that the TCC effect is non-negligible in the device thermal estimation.

B. Local Ambient-to-Global Ambient Thermal Modeling

As mentioned in (24), the local ambient temperature for each SM $T_{\mathrm{la}i}$ is the reference to estimate the junction/hotspot temperature of devices. The accuracy of the local ambient temperature affects the accuracy of the estimated device temperatures. The conventional thermal models usually assume the local ambient temperature as identical as the global ambient temperature. However, for the MMC with many SMs, the local ambient temperature of an SM is inevitably affected by the temperature rises of the neighboring subsystems as shown in Fig. 16. Thus, the SM and arm inductors are regarded as a unit. A thermal matrix method is applied again to consider the system-level TCC effects, which is expressed as

$$\mathbf{T}_{\mathrm{la}} = \mathbf{Z}_{\mathrm{a}} \mathbf{P}_{\mathrm{SM/L}} + T_{\mathrm{ga}} \qquad (25)$$

where $\mathbf{T}_{\mathrm{la}}$ is the local ambient temperature vector of each SM. The local ambient-to-global ambient thermal impedance $\mathbf{Z}_{\mathrm{a}}$ characterizes the TCC effects between SMs/inductors and the impact of the cabinet.

In this case, the local ambient-to-global ambient thermal impedances are also characterized by FEM simulations. Each SM is heated up separately, and the local ambient temperature of each SM is recorded. Then, the obtained transient thermal impedances are shown in Fig. 20. When SM1 on the backside of the cabinet is heated up, the rising of self-thermal impedance $Z_{\mathrm{a1,1}}$ indicates that the local ambient temperature of SM1 increases, as shown in Fig. 20(a). Meanwhile, the local ambient

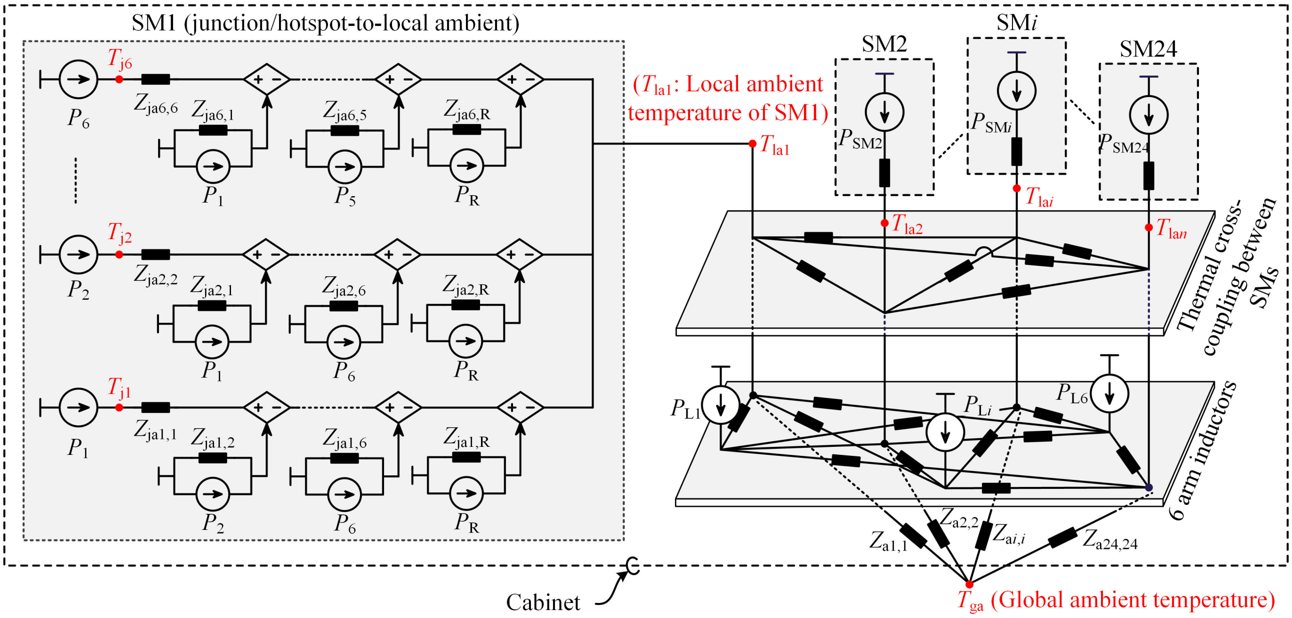

Fig. 16. Hierarchical decomposition of system-level thermal modeling of the down-scale MMC prototype, which considers the TCC effects among devices and among different subsystems. (T_{j1}–T_{j6} are junction/hotspot temperatures of power devices or capacitors, T_{lai} is the local ambient temperature of the ith SM, T_{ga} is the global ambient temperature of the environment, P_{SMi} is the total power losses of the ith SM, and P_{Li} is the ith arm-inductor power losses.)

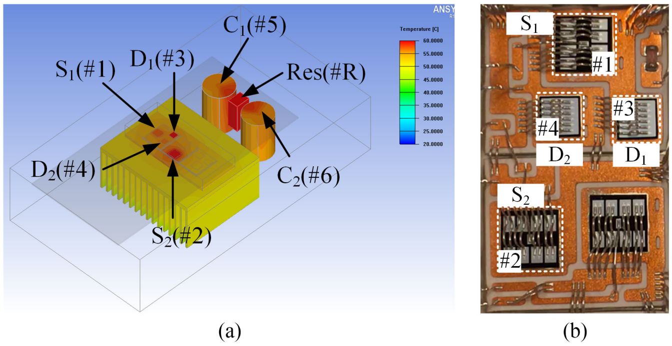

Fig. 17. Configuration of an SM. (a) FEM model. (a) Chip layout of the IGBT module.

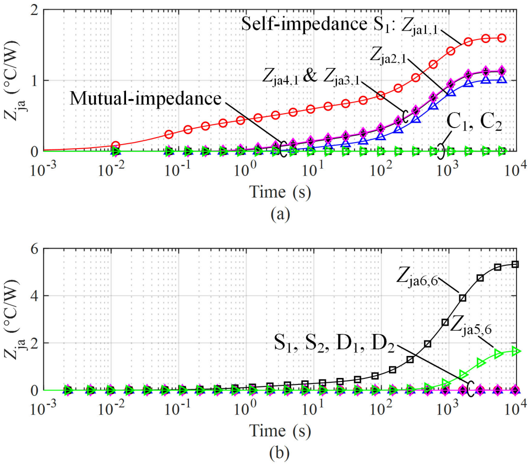

Fig. 18. FEM simulation results for the self-junction/hotspot-to-local ambient thermal impedances and mutual thermal impedances for the devices in an SM: (a) the active device S_1, and (b) the passive device C_2.

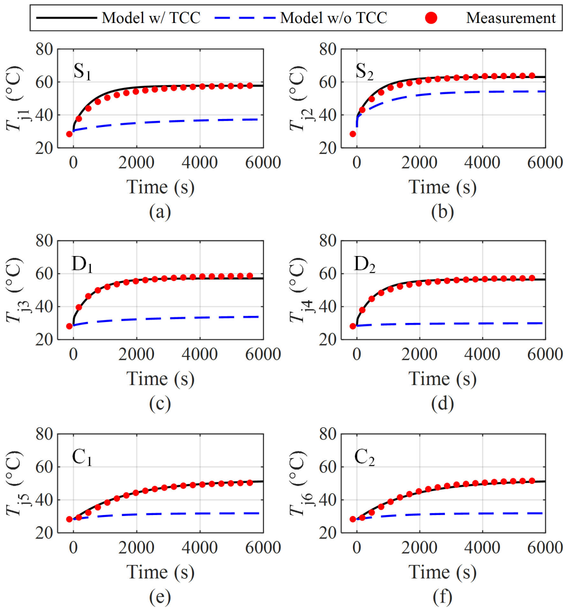

Fig. 19. Junction/hotspot temperatures of the critical devices in an SM (see Fig. 17): (a) S_1, (b) S_2, (c) D_1, (d) D_2, (e) C_1, and (f) C_2 (where T_{lamb}=28 °C, active and reactive power of the MMC are 13.5 kW and 6.5 kVar, respectively).

temperatures of the SMs (i.e., SM7, SM8, SM13, SM14, and SM19) are also heated up, which are described as the rising curves of $Z_{a7,1}$, $Z_{a8,1}$, $Z_{a13,1}$, $Z_{a14,1}$, and $Z_{a19,1}$. Since the cooling air is imported from the bottom and backside grilles and exhausts via the top of the cabinet, the TCC effects between SMs propagate mainly through the upward direction. Similarly, the front-side SM4 is heated up, as shown in Fig. 20(b). Compared to the SM1 in the same layer of the cabinet, the TCC effects of

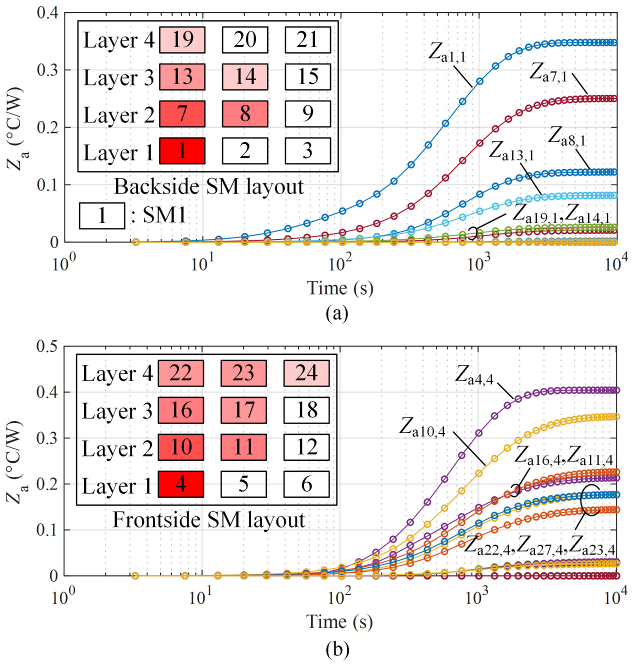

Fig. 20. Local ambient-to-global ambient thermal impedances with single SM heated-up, respectively. (a) SM1 is heated up only. (b) SM4 is heated up only.

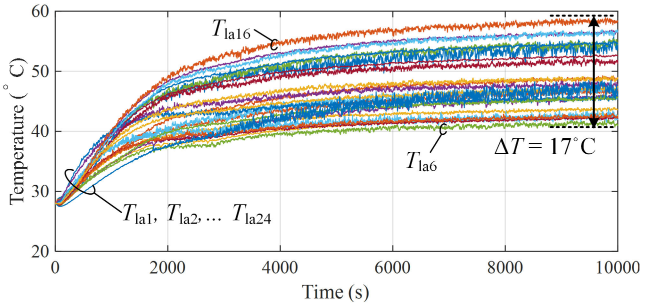

Fig. 21. Measured local ambient temperatures of 24 SMs in the MMC platform, where active and reactive powers are 13.5 kW and 6.5 kVar, and the global ambient temperature is 28 °C.

SM4 are more noticeable. This is because the front cabinet is airtight glass while the backside is grille with airflow. Thus, the properties of the cabinet also have a significant impact on the local ambient-to-global ambient thermal impedances. In summary, the local ambient temperatures of SMs are significantly affected by the layout, the cooling method, and the material properties of the cabinet.

To identify the local ambient temperature distribution of the cabinet, measurement is carried out on each SM using K-type thermocouples and a data logger NI-9213. The local ambient temperatures of the 24 SMs are monitored continuously, as shown in Fig. 21. When the MMC system is not running (Time = 0 s), all the local ambient temperatures are equal to the global ambient temperature of 28 °C. Afterward, the local ambient temperatures of the SMs are divergent with the system operating. The divergence between different SMs is up to 17 °C. Moreover, even though SM6 has the lowest local ambient temperature, $T_{\mathrm{la6}} = 41$ °C is still obviously higher than the global ambient temperature. Thus, without consideration of the difference between the local ambient temperature and the global ambient temperature, the estimated device stresses will be underestimated. Furthermore, Fig. 22 compares the measured local ambient temperatures to the estimated values. The estimated results agree with the experimental data, with a maximum error of 2.5%.

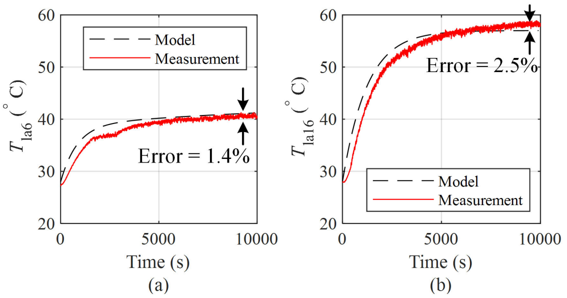

Fig. 22. Comparison of the measured local ambient temperatures and the estimated results of two SMs: (a) SM6, and (b) SM16 (the conditions are the same as Fig. 21).

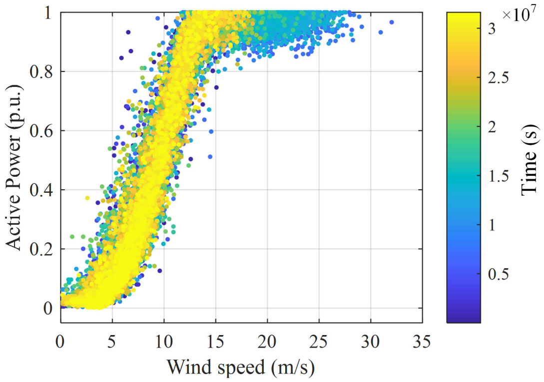

Fig. 23. Annual mission profile of wind speeds with 1 Hz sampling frequency and the corresponding converted active powers.

V. LIFETIME AND ACCUMULATED DAMAGE ANALYSIS

According to the comparison of the mission profiles with different resolutions in [30], an annual wind speed profile with 1 Hz sampling frequency is utilized in this article for reliability assessment. Following, the high-resolution wind speeds are converted into active powers, as shown in Fig. 23. The reactive power of the down-scale prototype is set to be constant at 6.5 kVar throughout the year. In this section, static annual damages of components are analyzed based on the mission profiles and the established electro-thermal models. Then, a Monte Carlo simulation is carried out to take all the parameter variations into account. The obtained failure probability of the components due to wear out contributes to getting the system-level reliability.

A. Thermal Profiles and Static Annual Damage of Components

Based on the established electro-thermal models, the annual mission profiles are converted into thermal profiles for each

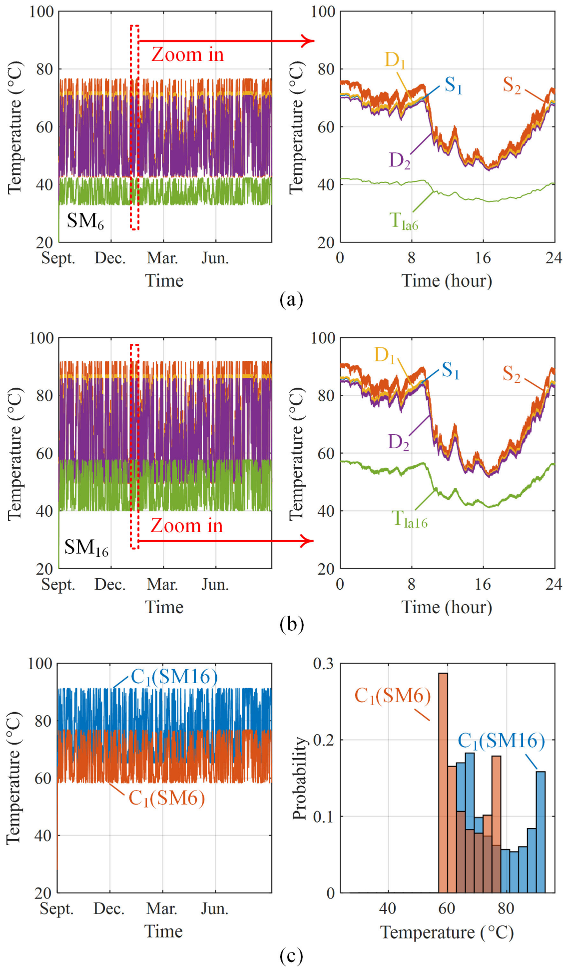

Fig. 24. Simulated temperatures for critical components (S_1, S_2, D_1, D_2, C_1) and local ambient temperatures for different SMs: (a) SM6, (b) SM16, and (c) capacitor hotspot temperatures in SM6 and SM16 and corresponding temperature distributions using an annual wind speed mission profile.

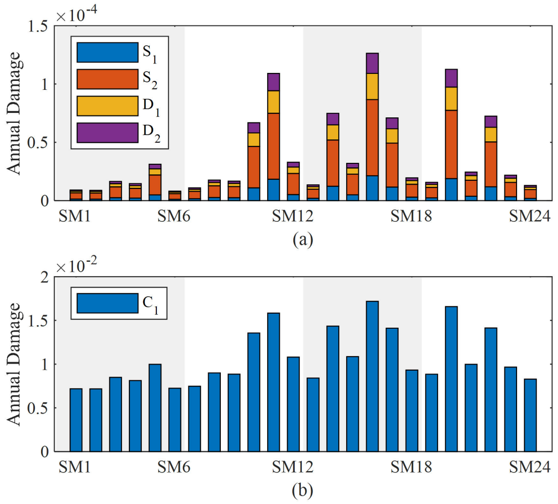

Fig. 25. Annual damages of each critical components in the 24 SMs. (a) Power semiconductor devices. (b) Capacitors.

component, as shown in Fig. 24. Although the global ambient temperature is 28 °C, the local ambient temperature of SM6 varies between 35–40 °C, as shown in Fig. 24(a). The junction temperatures of the power devices are fluctuating within the range of 40–75 °C. Due to the TCC effects among the power devices, the unbalanced power losses of the four power devices do not lead to a large difference between the junction temperatures. The junction temperature of S_2 is the highest while the other three junction temperatures are very close. When comparing the thermal profiles in SM16 [see Fig. 24(b)], both the local ambient temperature and the junction temperatures have higher variations, which reveals that the SMs of the MMC bear the different thermal stresses even if they have relatively equal power losses. As shown in Fig. 24(c), the capacitor thermal profiles and the thermal distributions also have similar phenomena.

The temperature fluctuations in the power semiconductor devices induce repetitive thermo-mechanical stresses, which in return accumulate as fatigue on the devices, and challenge the lifetime. According to the comparative study based on MMC applications [10] and the manufacturer provided data [31], the lifetime model for the selected IGBT module is

$$N_\mathrm{f} = A(\Delta T_\mathrm{j})^{\beta_1} \cdot \exp\left(\frac{\beta_2}{T_\mathrm{jmax}+273}\right) \cdot \left(\frac{t_\mathrm{on}}{1.5}\right)^{\beta_3} \tag{26}$$

where N_f is the number of cycles to failure, ΔT_j is the junction temperature swing, T_jmax is the maximum junction temperature, t_on is the power-on time, and A, β_1, β_2, and β_3 are fitting parameters. Based on [31], the parameters has $A = 1.42 \times 10^{12}$, $\beta_1 = -7.14$, $\beta_2 = 5154$, $\beta_3 = -0.3$, and t_on has limitations of $0.1\ \mathrm{s} < t_\mathrm{on} < 60\ \mathrm{s}$.

Moreover, the state-of-the-art lifetime model for Al-Caps is affected by the temperature stress and the voltage stress [32], which is given by

$$L_\mathrm{c} = L_\mathrm{c0} \cdot 2^{\frac{T_0 - T}{n_1}} \cdot \left(\frac{U}{U_0}\right)^{-n_2} \tag{27}$$

where L_c is the lifetime under the real thermal and electrical stresses T and U, while L_c0 is the lifetime under the reference thermal and electrical conditions T_0 and U_0. The coefficients n_1 and n_2 are a temperature dependent constant and a voltage stress exponent, respectively. In this case, the coefficient n_1 is 10 and the parameter n_2 is 5 according to [32].

The total damage to a device is accumulated based on Palmgren–Miners rules [33] as

$$D_\mathrm{mg} = \sum_k \frac{n_k}{N_{\mathrm{f}k}} \tag{28}$$

where n_k is the number of cycles associated with a specific stress, and $N_{\mathrm{f}k}$ is the number of cycles till failure for the same stress. The device fails when the accumulative D_mg reaches one.

The annual damages of IGBTs and capacitors of different SMs are shown in Fig. 25. Even if the same IGBT type is utilized, the annual accumulated damages due to wear-out of power devices are different for various SMs as shown in Fig. 25(a). The total damage of power devices in SM16 is up to 1.3×10^{-4} per year, while SM6 has 0.1×10^{-4} damage per year only. For a specific

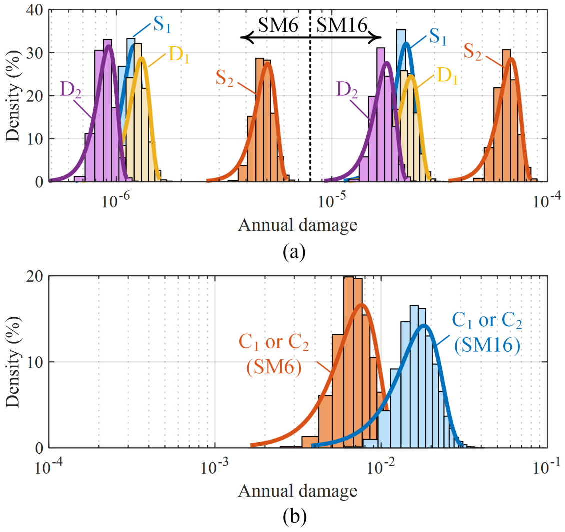

Fig. 26. Monte Carlo simulations of the critical components in SM6 and SM16. (a) Power semiconductor devices. (b) Capacitors.

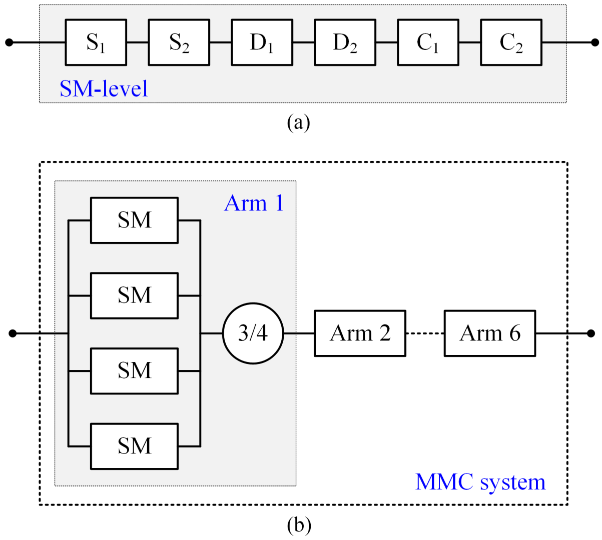

Fig. 27. System-level reliability calculation via reliability block diagram: (a) composition of power semiconductor devices and capacitors in an SM, and (b) composition of the entire MMC system, where the arm has 3-out-of-4 redundancy.

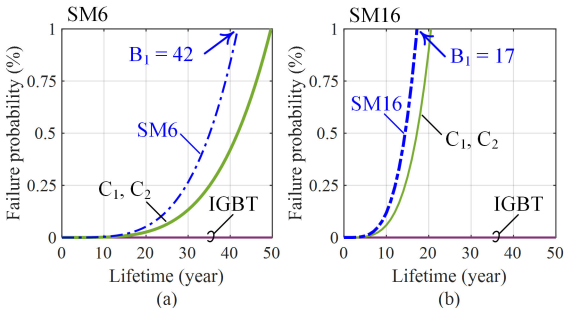

Fig. 28. Failure probability due to wear out of IGBTs and capacitors in two SMs. (a) SM6. (b) SM16.

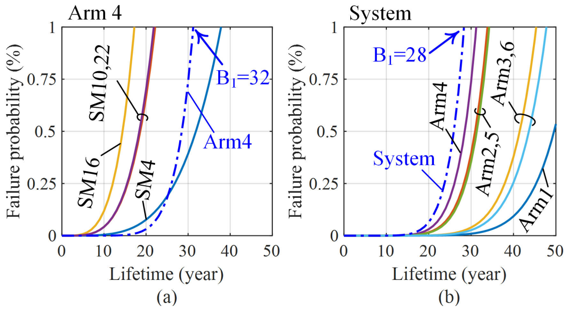

Fig. 29. Accumulated percentage of wear-out failure probability in the MMC system. (a) From the SM level to the arm level. (b) From the arm level to the system level.

SM, the device S_2 always has the largest annual damage since S_2 has the highest power losses in the MMC. On the other hand, the annual damages due to wear-out of capacitors are much more severe. A single capacitor in SM16 has a damage of 1.7×10^{-2} per year, which is almost 100 times the damages of power devices.

B. Monte Carlo Simulations and System-Level Failure Probability

The static damage is rarely practicable to anticipate all of device failures, thus, it is necessary to take the uncertainties involved into account as well. Monte Carlo simulations are conducted in this part to consider the impact of parameter variations, such as the varied parameters of the used devices as shown in Figs. 6, 9, and 11 and the various of the lifetime parameters in (26) and (27) (considering 95% confidence intervals). Consequently, the histograms of annual damages for the devices in SM6 and SM16 are shown in Fig. 26. In SM6, the device S_2 has the largest annual damage distribution, which is centered around 5×10^{-6} per year, as shown in Fig. 26(a). Meanwhile, the damage distributions of all the power devices in SM16 are larger than SM6 due to the relatively higher thermal stresses. Similarly, the annual damages of capacitors in SM16 are also larger than the ones in SM6, as shown in Fig. 26(b), but the capacitor damages ranging around 1×10^{-2} per year significantly surpass the power semiconductors. Accordingly, the histograms are fitted with the Weibull distribution as

$$f(t) = \frac{\beta}{\eta}\left(\frac{t}{\eta}\right)^{\beta-1} e^{-\left(\frac{t}{\eta}\right)^{\beta}}, \quad F(t) = 1 - e^{-\left(\frac{t}{\eta}\right)^{\beta}} \tag{29}$$

where β is the shape parameter and η is the scale parameter.

Following, the reliability assessment of the MMC follows the steps from the SM level, the arm level, to the entire system. The reliability block diagram (RBD) to calculate the reliability function is shown in Fig. 27. For the reliability analysis of an SM, any failed power semiconductor or capacitor results in abnormal operation of the SM, which indicates that all the power devices and capacitors are serially connected in the RBD, as shown in Fig. 27(a). Therefore, the failure function $F_{\mathrm{SM}i}$ and reliability function $R_{\mathrm{SM}i}$ of the ith SM are expressed by the component

TABLE IV
COMPARISON OF THE DOWN-SCALE PROTOTYPE AND FULL-SCALE MMC SYSTEMS AND CORRESPONDING REFERENCES

Categories	Down-scale prototype	Full-scale MMC	References
Power semiconductors	Stacked packaging IGBT modules	Press-pack IGBT devices	[35], [36]
		IGCT	[37]
Capacitors	Al-capacitors	Film capacitors	[20], [36]
Magnetic components	Iron-core inductors	Air-core inductors	[43]
Cooling methods	Forced air-cooling	Liquid cooling	[39]
Other components	None	Optical fibers	[40]
		Control board	[41]
		Mechanical parts	[42]

failure function $F_{\mathrm{com}j}$

$$F_{\mathrm{SM}i}(t) = 1 - \prod_{j=1}^{6} \left[1 - F_{\mathrm{com}j}(t)\right] \tag{30}$$

$$R_{\mathrm{SM}i}(t) = \prod_{j=1}^{6} \left[1 - F_{\mathrm{com}i}(t)\right]. \tag{31}$$

Based on the component failure rates of SM6 and SM16, the corresponding wear-out failure probability is shown in Fig. 28. The failure probabilities of IGBTs/diodes of the both SMs are almost zero while the damages of capacitors are rapidly soaring. It implies that the power devices have excessive design margins in the case. The B_1 lifetimes (1% devices fail) of the capacitors in SM6 and SM16 are within 50 and 20 years, respectively. Meanwhile, the B_1 lifetimes of SM6 and SM16 due to wear out are within 42 and 17 years, respectively. The lifetime of the SMs is dominated by the reliability of capacitors.

Afterward, the reliability analysis of the entire MMC system is shown in Fig. 27(b). In each arm, a 3-out-of-4 redundancy is applied to improve the reliable performance. Taking the first arm as an example, which consists of SM1, SM7, SM13, and SM19, the failure function of the arm is expressed as

$$\begin{aligned} F_{\mathrm{arm1}}(t) = 1 &- R_{\mathrm{SM1}}(t)R_{\mathrm{SM7}}(t)R_{\mathrm{SM13}}(t)R_{\mathrm{SM19}}(t) \\ &- F_{\mathrm{SM1}}(t)R_{\mathrm{SM7}}(t)R_{\mathrm{SM13}}(t)R_{\mathrm{SM19}}(t) \\ &- R_{\mathrm{SM1}}(t)F_{\mathrm{SM7}}(t)R_{\mathrm{SM13}}(t)R_{\mathrm{SM19}}(t) \\ &- R_{\mathrm{SM1}}(t)R_{\mathrm{SM7}}(t)F_{\mathrm{SM13}}(t)R_{\mathrm{SM19}}(t) \\ &- R_{\mathrm{SM1}}(t)R_{\mathrm{SM7}}(t)R_{\mathrm{SM13}}(t)F_{\mathrm{SM19}}(t). \end{aligned} \tag{32}$$

Furthermore, the system-level reliability is a serial connection of six arms. The failure function, thus, is estimated by

$$F_{\mathrm{system}}(t) = 1 - \prod_{j=1}^{6} \left[1 - F_{\mathrm{arm}i}(t)\right]. \tag{33}$$

The corresponding arm-level and system-level reliability results are shown in Fig. 29. In Fig. 29(a), four different SMs have variable failure probabilities. Due to the redundant structure, the failure probability of the arm is smaller than all the consisting SMs in the first 25 years. After the 25th year, the unreliability is soaring and surpasses the failure probability of SM4. The B_1 lifetime of the arm is within 32 years. On the other hand, Fig. 29(b) depicts reliable relationship between each arm and the system. Arm 1 has the lowest failure probability while Arm 4 has the worst reliability in the entire system. Since the whole system is a serial connection, the reliability of the entire system is worse than all arms. The B_1 lifetime of the MMC is within 28 years. So far, the reliability assessment of the whole MMC platform has been established, which covers from single components to the composition of the SM and the arm.

VI. DISCUSSION

The article limits its scope to the wear-out failure of IGBTs and capacitors. It provides a potential method to size IGBTs and capacitors according to mission profile-based reliability prediction. It also demonstrates a systematic methodology to perform reliability analysis from system-level modeling to component-level modeling, and then, back to the system-level. The same method could be applied to other types of components.

Table IV lists the differences between the down-scale prototype and full-scale MMC systems. A typical full-scale MMC utilizes 4.5 kV/1.2 kA power modules [34], instead of the power module of 1.2 kV/50 A in the prototype. Meanwhile, other options for power devices usually have press-pack IGBTs, IGCT, etc. [35]–[37]. For passive components, full-scale MMC systems use more high-power film capacitors as they provide higher voltage ratings and better reliability performance [20]. The different failure mechanisms are necessary to be considered in terms of different packaging technologies and devices.

Moreover, the used static RBD model is limited to consider the dependence of failures among components/subsystems or the parameter degradation of components. More enhanced analysis requires methods such as dynamic RBD [38], etc., to make the assessment results more realistic.

Besides, single-event related failure of MMC is also an important part to be considered in the design and system-level reliability analysis, such as liquid cooling systems [39], optical fibers [40], control boards [41], mechanical parts [42], etc. It relies more on the field operation experiences of the specific type of MMCs or similar products. From the design perspective, proper protection strategies and robustness design are beneficial to the reduction of this type of failure.

VII. CONCLUSION

Based on a 15-kVA experimental prototype, this article provides a system-level methodology to assess the reliability of the MMC, covering the critical components, subsystems, and the entire system. The physics-of-failure methods are utilized according to three aspects: power loss models, thermal models, and lifetime models. In the power loss model, an analytical model has been established based on P/Q information at the PCC. All the selected components are measured, and the uneven parameters are considered. Moreover, a system-level thermal model is proposed through two parts: the junction/hotspot-to-local ambient thermal model and the local ambient-to-global ambient thermal model. The first part considers the TCC effects between different devices (e.g., IGBTs, capacitors, etc.). The measurements show the TCC effects significantly affect the thermal estimation, an error of 45% is observed based on the conventional thermal models without considering TCC effects. Subsequently, the second part of the thermal model provides a more accurate temperature reference for each SM. An *in situ* measurement has revealed that not only the local ambient temperatures are different from the global ambient temperature up to 30 °C, but also the local ambient temperatures between SMs are divergent to each other (up to 17 °C). Even though the same type of components are utilized in each SM and the power losses between SMs are homogeneous, the divergent thermal results reveal the complicated thermal behaviors in the MMC. Finally, a long-term mission profile is utilized to evaluate the reliability of the MMC. The diverse annual damages among devices and SMs comprehensively illustrate the impacts of the uneven parameters and the complicated thermal behaviors in the MMC. The annual damage of a single component is as low as 1×10^{-6} per year, but the lifetime of the system due to wear-out failures is within 28 years only. This phenomenon emphasizes the severe reliability challenges in the MMC in terms of components and system integrations. The results also provide a guideline for the sizing of key components and the physical layout of SMs.

REFERENCES

[1] S. Debnath, J. Qin, B. Bahrani, M. Saeedifard, and P. Barbosa, “Operation, control, and applications of the modular multilevel converter: A review,” *IEEE Trans. Power Electron.*, vol. 30, no. 1, pp. 37–53, Jan. 2015.

[2] S. Yang, A. Bryant, P. Mawby, D. Xiang, L. Ran, and P. Tavner, “An industry-based survey of reliability in power electronic converters,” *IEEE Trans. Ind. Appl.*, vol. 47, no. 3, pp. 1441–1451, Mar. 2011.

[3] G. Konstantinou, J. Pou, S. Ceballos, and V. G. Agelidis, “Active redundant submodule configuration in modular multilevel converters,” *IEEE Trans. Power Del.*, vol. 28, no. 4, pp. 2333–2341, Oct. 2013.

[4] O. Cwikowski, H. R. Wickramasinghe, G. Konstantinou, J. Pou, M. Barnes, and R. Shuttleworth, “Modular multilevel converter DC fault protection,” *IEEE Trans. Power Del.*, vol. 33, no. 1, pp. 291–300, Feb. 2017.

[5] B. Wang, X. Wang, Z. Bie, P. D. Judge, X. Wang, and T. C. Green, “Reliability model of MMC considering periodic preventive maintenance,” *IEEE Trans. Power Del.*, vol. 32, no. 3, pp. 1535–1544, Jun. 2017.

[6] J. Xu, P. Zhao, and C. Zhao, “Reliability analysis and redundancy configuration of MMC with hybrid submodule topologies,” *IEEE Trans. Power Electron.*, vol. 31, no. 4, pp. 2720–2729, Apr. 2016.

[7] P. Tu, S. Yang, and P. Wang, “Reliability- and cost-based redundancy design for modular multilevel converter,” *IEEE Trans. Ind. Electron.*, vol. 66, no. 3, pp. 2333–2342, Mar. 2019.

[8] “Military handbook: Reliability prediction of electronic equipment MIL-HDBK-217F,” Dept. Def. USA, Tech. Rep. MIL-HDBK-217, 1991.

[9] H. Liu, K. Ma, Z. Qin, P. C. Loh, and F. Blaabjerg, “Lifetime estimation of MMC for offshore wind power HVDC application,” *IEEE J. Emerg. Sel. Topics Power Electron.*, vol. 4, no. 2, pp. 504–511, Sep. 2016.

[10] Y. Zhang, H. Wang, Z. Wang, Y. Yang, and F. Blaabjerg, “Impact of lifetime model selections on the reliability prediction of IGBT modules in modular multilevel converters,” in *Proc. IEEE Energy Convers. Congr. Expo.*, 2017, pp. 4202–4207.

[11] *Determination of Power Losses in Voltage Sourced Converter (VSC) Valves for HVDC Systems—Part 2: Modular Multilevel Converters*, IEC-62751-2, 2012.

[12] H. Wang, G. Tang, Z. He, and J. Cao, “Power loss and junction temperature analysis in the modular multilevel converters for HVDC transmission systems,” *J. Power Electron.*, vol. 15, no. 3, pp. 685–694, May 2015.

[13] T. Modeer, H. P. Nee, and S. Norrga, “Loss comparison of different sub-module implementations for modular multilevel converters in HVDC applications,” *Eur. Power Electron. Drives*, vol. 22, no. 3, pp. 32–38, Sep. 2012.

[14] Z. Zhang, Z. Xu, and Y. Xue, “Valve losses evaluation based on piecewise analytical method for MMC-HVDC links,” *IEEE Trans. Power Del.*, vol. 29, no. 3, pp. 1354–1362, Jun. 2014.

[15] F. Hahn, M. Andresen, G. Buticchi, and M. Liserre, “Thermal analysis and balancing for modular multilevel converters in HVDC applications,” *IEEE Trans. Power Electron.*, vol. 33, no. 3, pp. 1985–1996, Mar. 2018.

[16] W. Li *et al.*, “Thermal optimization of modular multilevel converters with surplus sub-module active-bypass plus neutral-point-shift scheme under unbalanced grid,” *IEEE J. Emerg. Sel. Topics Power Electron.*, vol. 7, no. 3, pp. 1777–1788, Sep. 2019.

[17] J. Goncalves, D. J. Rogers, and J. Liang, “Submodule temperature regulation and balancing in modular multilevel converters,” *IEEE Trans. Ind. Electron.*, vol. 65, no. 9, pp. 7085–7094, Sep. 2018.

[18] Y. Dong, H. Yang, W. Li, and X. He, “Neutral-point-shift-based active thermal control for a modular multilevel converter under a single-phase-to-ground fault,” *IEEE Trans. Ind. Electron.*, vol. 66, no. 3, pp. 2474–2484, Mar. 2019.

[19] S. Thomas, “Infineon AN2008-03: Thermal equivalent circuit models,” Tech. Rep., 2008.

[20] H. Wang and F. Blaabjerg, “Reliability of capacitors for DC-link applications in power electronic convertersan overview,” *IEEE Trans. Ind. Appl.*, vol. 50, no. 5, pp. 3569–3578, Sep./Oct. 2014.

[21] D. Zhou, H. Wang, and F. Blaabjerg, “Mission profile based system-level reliability analysis of DC/DC converters for a backup power application,” *IEEE Trans. Power Electron.*, vol. 33, no. 9, pp. 8030–8039, Aug. 2018.

[22] Y. Shen, A. Chub, H. Wang, D. Vinnikov, E. Liivik, and F. Blaabjerg, “Wear-out failure analysis of an impedance-source PV microinverter based on system-level electrothermal modeling,” *IEEE Trans. Ind. Electron.*, vol. 66, no. 5, pp. 3914–3927, May 2019.

[23] C. Oates, “Modular multilevel converter design for VSC HVDC applications,” *IEEE J. Emerg. Sel. Top. Power Electron.*, vol. 3, no. 2, pp. 505–515, Jun. 2015.

[24] P. D. Judge, G. Chaffey, M. M. Merlin, P. R. Clemow, and T. C. Green, “Dimensioning and modulation index selection for the hybrid modular multilevel converter,” *IEEE Trans. Power Electron.*, vol. 33, no. 5, pp. 3837–3851, May 2018.

[25] K. Ilves, A. Antonopoulos, S. Norrga, and H. P. Nee, “Steady-state analysis of interaction between harmonic components of arm and line quantities of modular multilevel converters,” *IEEE Trans. Power Electron.*, vol. 27, no. 1, pp. 57–68, Jan. 2012.

[26] T. Nakanishi and J. I. Itoh, “High power density design for a modular multilevel converter with an H-bridge cell based on a volume evaluation of each component,” *IEEE Trans. Power Electron.*, vol. 33, no. 3, pp. 1967–1984, Mar. 2018.

[27] Y. Zhang, H. Wang, Z. Wang, Y. Yang, and F. Blaabjerg, “Simplified thermal modeling for IGBT modules with periodic power loss profiles in modular multilevel converters,” *IEEE Trans. Ind. Electron.*, vol. 66, no. 3, pp. 2323–2332, Apr. 2018.

[28] *Maxwell Online Help*, ANSYS, Canonsburg, PA, USA, 2016.

[29] K. Ma, M. Liserre, F. Blaabjerg, and T. Kerekes, “Thermal loading and lifetime estimation for power device considering mission profiles in wind power converter,” *IEEE Trans. Power Electron.*, vol. 30, no. 2, pp. 590–602, Mar. 2015.

[30] Y. Zhang, H. Wang, Z. Wang, Y. Yang, and F. Blaabjerg, “The impact of mission profile models on the predicted lifetime of IGBT modules in the modular multilevel converter,” in *Proc. 43rd Annu. Conf. IEEE Ind. Electron. Soc.*, 2017, pp. 7980–7985.

[31] H. Ludwig, “AN2010-02 technical information: IGBT modules use of power cycling curves for IGBT4,” Tech. Rep. AN2010-02, pp. 1–6, 2010.

[32] D. Zhou, Y. Song, Y. Liu, and F. Blaabjerg, “Mission profile based reliability evaluation of capacitor banks in wind power converters,” *IEEE Trans. Power Electron.*, vol. 34, no. 5, pp. 4665–4677, May 2019.

[33] M. A. Miner, “Cumulative damage in fatigue,” *Amer. Soc. Mech. Engineers, J. Appl. Mechanics*, vol. 12, pp. 159–164, 1945.

[34] K. Sharifabadi, L. Harnefors, H.-P. Nee, R. Teodorescu, and S. Norrga, *Design, Control and Application of Modular Multilevel Converters for HVDC Transmission Systems*. Hoboken, NJ, USA: Wiley, 2016.

[35] H. Y. Long, M. R. Sweet, E. M. S. Narayanan, and G. Li, "Reliability study and modelling of IGBT press-pack power modules," in *Proc. IEEE Appl. Power Electron. Conf. Expo.*, Mar. 2017, pp. 2711–2717.

[36] L. Hui *et al.*, "Reliability modelling and analysis on MMC for VSC-HVDC by considering the press-pack IGBT and capacitors failure," *J. Eng.*, vol. 2019, no. 16, pp. 2219–2223, 2019.

[37] B. Zhao *et al.*, "A more prospective look at IGCT: uncovering a promising choice for dc grids," *IEEE Ind. Electron. Mag.*, vol. 12, no. 3, pp. 6–18, Sep. 2018.

[38] S. Distefano and A. Puliafito, "Dependability evaluation with dynamic reliability block diagrams and dynamic fault trees," *IEEE Trans. Dependable Secur. Comput.*, vol. 6, no. 1, pp. 4–17, Jan.–Mar. 2009.

[39] G. Bing, H. Tingting, Y. Fan, L. Chao, S. Xiaoning, and C. Yijie, "Investigation on deposition behavior of HVDC water cooling system based on electro-mass transfer-velocity coupling model," *IEEE Access*, vol. 7, pp. 1–1, 2019.

[40] N. Evano, R. El Abdi, and M. Poulain, "Lifetime modeling of silica optical fiber in static fatigue test," *J. Appl. Res. Technol.*, vol. 14, no. 4, pp. 278–285, 2016.

[41] R. Grinberg, G. Riedel, A. Korn, P. Steimer, and E. Bjornstad, "On reliability of medium voltage multilevel converters," in *Proc. IEEE Energy Convers. Congr. Expo.*, 2013, pp. 4047–4052.

[42] M. Hook, "Calculating target availability figures for HVDC interconnectors," Tech. Rep. VP01244, 2012.

[43] Z. Yuan *et al.*, "Thermal analysis of air-core power reactors," *ISRN Mech. Eng.*, vol. 2013, pp. 1–7, 2013.

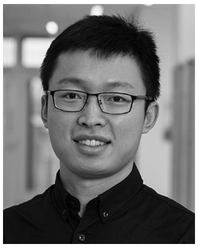

Yi Zhang (S'17) received the B.S. and M.S. degrees in electrical engineering from Harbin Institute of Technology, Harbin, China, in 2014 and 2016, respectively. He is currently working toward the Ph.D. degree with Aalborg University, Aalborg, Denmark.

He was a visiting scholar with Georgia Institute of Technology, Atlanta, GA, USA, from November 2018 to February 2019. His current research interests include the reliability of power electronic devices and applications, and multilevel converters.

Huai Wang (M'12–SM'17) received the B.E. degree in electrical engineering from the Huazhong University of Science and Technology, Wuhan, China, in 2007, and the Ph.D. degree in power electronics from the City University of Hong Kong, Hong Kong, in 2012.

He is currently a Professor with the Center of Reliable Power Electronics, Department of Energy Technology, Aalborg University, Denmark. He was a Visiting Scientist with ETH Zurich, Switzerland, from August to September 2014, and with the Massachusetts Institute of Technology, USA, from September to November 2013. He was with ABB Corporate Research Center, Switzerland, in 2009. His research interests include the fundamental challenges in modeling and validation of power electronic component failure mechanisms, and application issues in system-level predictability, condition monitoring, circuit architecture, and robustness design.

Dr. Wang is the recipient of the Richard M. Bass Outstanding Young Power Electronics Engineer Award from the IEEE Power Electronics Society in 2016, and the Green Talents Award from the German Federal Ministry of Education and Research in 2014. He is currently the Chair of IEEE Power Electronics Society/Industry Applications Society/Industrial Electronics Society Chapter in Denmark. He serves as an Associate Editor for IET Electronics Letters, IEEE Journal of Emerging and Selected Topics in Power Electronics, and IEEE Transactions on Power Electronics.

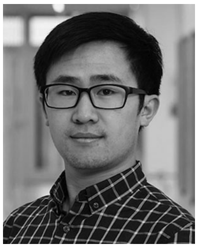

Zhongxu Wang (S'17) received the bachelor's and master's degrees in electrical engineering from the Harbin Institute of Technology, Harbin, China, in 2014 and 2016, respectively. He is currently working toward the Ph.D. degree with Aalborg University, Aalborg, Denmark.

In 2018, he was a Visiting Researcher with the Energy Futures Lab, Imperial College London, U.K. His research interests include the reliability improvement strategies of modular multilevel converters, including power balancing control, adaptive control, and condition monitoring of MMC.

Frede Blaabjerg (S'86–M'88–SM'97–F'03) received the Ph.D. degree in electrical engineering from Aalborg University, Aalborg, Denmark, in 1995.

From 1987 to 1988, he was with ABB-Scandia, Randers, Denmark. He became an Assistant Professor in 1992, an Associate Professor in 1996, and a Full Professor of Power Electronics and Drives in 1998. In 2017, he became a Villum Investigator. He is honoris causa with the University Politehnica Timisoara, Romania and Tallinn Technical University, Estonia. He has authored and coauthored more than 600 journal papers in the fields of power electronics and its applications. He is the co-author of four monographs and editor of ten books in power electronics and its applications. His current research interests include power electronics and its applications such as in wind turbines, PV systems, reliability, harmonics, and adjustable speed drives.

Prof. Blaabjerg is the recipient of 32 IEEE Prize Paper Awards, the IEEE PELS Distinguished Service Award in 2009, the EPE-PEMC Council Award in 2010, the IEEE William E. Newell Power Electronics Award 2014, the Villum Kann Rasmussen Research Award 2014, the Global Energy Prize in 2019, and the 2020 IEEE Edison Medal. He was the Editor-in-Chief of the IEEE Transactions on Power Electronics from 2006 to 2012. He was Distinguished Lecturer for the IEEE Power Electronics Society from 2005 to 2007 and for the IEEE Industry Applications Society from 2010 to 2011 as well as 2017 to 2018. Since 2019, he has been the President for the IEEE Power Electronics Society. He is the Vice-President of the Danish Academy of Technical Sciences too. He is nominated in 2014–2018 by Thomson Reuters to be among the most 250 cited researchers in Engineering in the world.

Maryam Saeedifard (SM'11) received the Ph.D. degree in electrical engineering from the University of Toronto, Toronto, ON, Canada, in 2008.

She is currently an Associate Professor with the School of Electrical and Computer Engineering, Georgia Institute of Technology, Atlanta, GA, USA. Prior joining Georgia Tech, she was an Assistant Professor with the School of Electrical and Computer Engineering, Purdue University, West Lafayette, IN, USA. Her research interests include power electronics and applications of power electronics in power systems.